

EUROPEAN COMMISSION

HORIZON 2020 PROGRAMME
TOPIC H2020-LCE-07-2016-2017

Developing the next generation technologies of renewable electricity and
heating/cooling

GA No. 727523

**Next – generation interdigitated back-contacted silicon
heterojunction solar cells and modules by design and
process innovations**



NextBase - Deliverable report

**D4.2 – IBC devices with transition metal oxide (TMO)
based contact stacks with $V_{oc} > 740$ mV and $FF > 82\%$**

Deliverable No.	NextBase D4.2	
Related WP	WP4	
Deliverable Title	IBC devices with TMO based contact stacks with $V_{oc}>740$ mV and $FF>82\%$	
Deliverable Date	2019-09-30	
Deliverable Type	DEM	
Dissemination level	Public (PU)	
Author(s)	Lars Korte (HZB), Mathieu Boccard (EPFL)	2019-09-15
Checked by	Frank Versluis (UNR)	2019-09-18
Reviewed by (if applicable)	Kaining Ding (Jülich) - Coordinator	2019-09-20
Approved by	Kaining Ding (Jülich) - Coordinator	2019-09-23
Status	Final	2019-09-23

Disclaimer/ Acknowledgment



Copyright ©, all rights reserved. This document or any part thereof may not be made public or disclosed, copied or otherwise reproduced or used in any form or by any means, without prior permission in writing from the NextBase Consortium. Neither the NextBase Consortium nor any of its members, their officers, employees or agents shall be liable or responsible, in negligence or otherwise, for any loss, damage or expense whatever sustained by any person as a result of the use, in any manner or form, of any knowledge, information or data contained in this document, or due to any inaccuracy, omission or error therein contained.

All Intellectual Property Rights, know-how and information provided by and/or arising from this document, such as designs, documentation, as well as preparatory material in that regard, is and shall remain the exclusive property of the NextBase Consortium and any of its members or its licensors. Nothing contained in this document shall give, or shall be construed as giving, any right, title, ownership, interest, license or any other right in or to any IP, know-how and information.

This project has received funding from the European Union's Horizon 2020 research and innovation programme under grant agreement No 727523. The information and views set out in this publication does not necessarily reflect the official opinion of the European Commission. Neither the European Union institutions and bodies nor any person acting on their behalf, may be held responsible for the use which may be made of the information contained therein.

Contents

1	Introduction.....	5
2	IBC cells with carrier-selective metal oxide contacts	6
3	Electron contact layers	7
3.1	Zinc oxide (ZnO).....	7
3.2	Tin oxide (SnO _x)	8
3.3	Magnesium oxide (MgO _x).....	11
4	Hole contact layers.....	14
4.1	Tungsten Oxide (WO _x)	14
	Sputtered tungsten oxide (WO _x)	14
	PEALD-deposited Tungsten Oxide	17
4.2	Indium Tungsten Oxide (IWO _x)	18
5	Summary of experimental results	23
6	Risks and interconnections.....	25
6.1	Risks/problems encountered	25
6.2	Interconnections with other deliverables	25
7	Conclusions.....	26
8	References.....	27

List of acronyms, abbreviations and definitions

Table 1.1 Acronym table

Abbreviation	Explanation
α-Si:H	Hydrogenated amorphous silicon
Ag	Silver
ARC	Anti-reflection coating
μc-Si	Microcrystalline silicon
μc-SiC	Microcrystalline silicon carbide
Cat-doping	Catalytic doping
CSC	Carrier-selective contact
dsp	Double-side polished
dst	Double-side textured
EQE(λ)	Wavelength-dependent external quantum efficiency
FF	Fill factor
FSF	Front surface field
HWCVD	Hot wire chemical vapor deposition
IQE	Internal quantum efficiency
ITO	Indium tin oxide
IBC	Interdigitated back contact
iVoc	Implied open circuit voltage
IWOx	Indium tungsten oxide
λ	Wavelength
J_{sc}	Short circuit current
j_{sc}	Short circuit current density
MgOx	Magnesium oxide
MoOx	Molybdenum oxide
MST	Modulated surface texture
PEALD	Plasma-enhanced atomic layer deposition
PECVD	Plasma enhanced chemical vapour deposition
R	Reflectance
SiN_x	Silicon nitride
SiO₂	Silicon oxide
SHJ	Silicon heterojunction
T	Transmittance
TMO	Transition metal oxide
V_{oc}	Open circuit voltage
WOx	Tungsten oxide
ZnO	Zinc oxide

1 Introduction

The deliverable “D4.2 – IBC devices with transition metal oxide (TMO) based contact stacks with $V_{oc}>740$ mV and $FF>82\%$ ” is part of NextBase’s WP4 “Novel layer stacks and contacting materials”. It is connected to T4.2 “Development and optimization of novel TMOs for selective contacts”, which aims at exploring a wide range of potential contact materials. The goal of the deliverable is to demonstrate the implementation of these alternative charge selective junctions in highly efficient IBC silicon heterojunction solar cells, in order to improve cell performance by reducing transport losses. Furthermore, such TMOs can be deposited by sputtering, thermal evaporation or ALD, which might provide cost advantages over conventional PECVD-deposited a-Si:H contacts.

Deliverable Number	Deliverable name	Lead partner	Type	Dissemination level	Due date
D4.2	IBC devices with TMO based contact stacks with $V_{oc}>740$ mV and $FF>82\%$	HZB	DEM	PU	M36

Chapter 2 reports on the fabrication of the currently best IBC cells with non-silicon carrier-selective contacts manufactured in the NextBase consortium, which show an efficiency of 22.2%. They were realized with molybdenum oxide, MoO_x , for the hole- and magnesium fluoride, MgF_x , for the electron-selective contact. These materials have also been used previously in double-side contacted CSC based silicon solar cells [1]. Unfortunately, despite the encouraging initial performance, stability of this device was unsatisfactory, as also acknowledged by previous authors.

Motivated by these findings, both project partners involved in T4.2 / D4.2, EPFL and HZB, have devoted considerable effort to exploring various alternative potential contact materials. Based on an initial literature review, the most promising candidate materials were selected from a wide range of available materials, e.g. for the electron contacts: TiO_x , ZnO_x , SnO_x , LiF_x , CsF_x , KF_x , CsO_x ; for the hole contacts: MoO_x , CuO_x , WO_x , NiO_x . Chapters 3 and 4 provide details on the properties of the most promising electron and hole contact materials investigated within the project including proof-of-concept implementations of such films in both side contacted heterojunction cells. Chapter 5 summarizes the reported results.

2 IBC cells with carrier-selective metal oxide contacts

The following figure presents the currently best IBC cell demonstrated to date with non-silicon carrier-selective contacts. It was manufactured within NextBase with a shadow mask process for IBC structuring, a full area (i)a-Si:H passivation, MoO_x/Ag stack for the hole- and MgF_x/Mg/Al/Ag stack for the electron-selective contact. It has the following device parameters, measured at STC: V_{oc} 709 mV, j_{sc} 41.5 mA/cm², FF 75.6%, power conversion efficiency 22.2% [2].

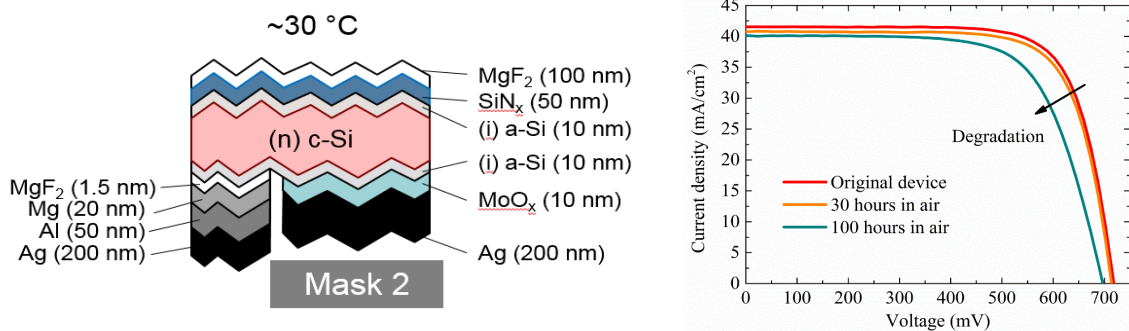


Figure 1. Left: IBC-SHJ cell with TMO contacts for both holes and electrons. Left: Device structure. Right: Illuminated I-V curves for the best cell, initially and after 30 & 100 hours in air.

This remarkable result surpasses the best previously published silicon cell with non-silicon contacts in literature, which is also a both-side contacted device, i.e. a simpler structure: Bullock's DASH cell [3] uses MoO_x and TiO_x/LiF as contact materials and achieves V_{oc} 706 mV, j_{sc} 38.4 mA/cm², FF 76%, PCE 20.7%. A relatively fast degradation however occurred upon waiting in air, which can come from the uncapped (i)a-Si:H layer in the gap between n and p contacts or to detrimental material interaction in the electron stack [3]. Also, the moderate contact selectivity, relatively high contact resistance and strong infrared-light parasitic absorption at the rear fundamentally limit the efficiency of this device. This indicates that optimization of the current design can lead to only marginal improvements, and alternative material stacks are required to reach 26% efficiency.

Our efforts towards identifying such candidate materials are summarized in the following chapters.

3 Electron contact layers

3.1 Zinc oxide (ZnO)

We investigated the possible use of Al-doped ZnO (AZO) cosputtered with SiO₂ as an electron contact layer, in view of its relatively low work function yet good conductivity. This combination presumably enables the use of relatively thick (>10 nm) films in TMO-based electron-selective contact stacks. AZO:SiO₂ is also expected to be less reactive with the surrounding Si or metal layers than nanometer-thin fluoride compounds. Layers of various thicknesses and with several compositions of AZO:SiO₂ were fabricated and investigated with various capping metals as electron-selective contacts in 2-side-contacted solar cells, as sketched in Figure 2. Main results are that optimal thickness and efficiency is roughly independent of the composition, and the capping metal has a strong influence on the selectivity of the contact. This highlights that AZO:SiO₂ cannot be a high-performance electron-selective contact, and that further material research is required to evidence one that could be.

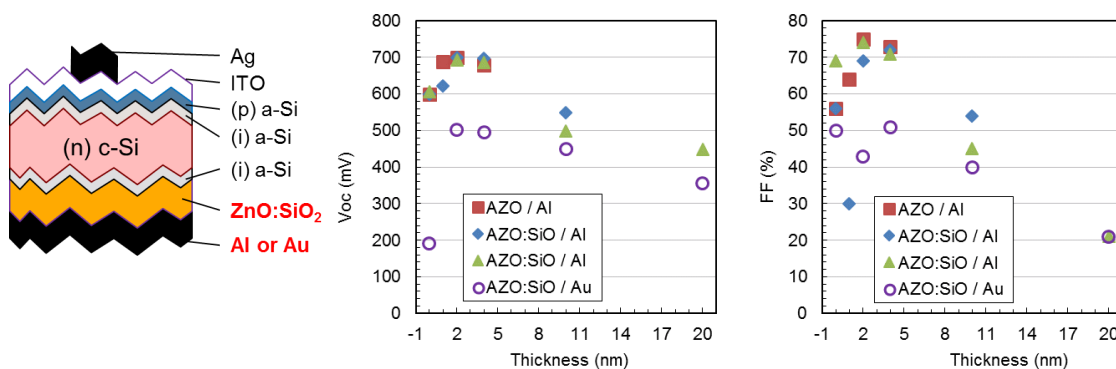


Figure 2 Sketch of the devices used to probe the ZnO:SiO₂ contact, and V_{oc} and FF of the resulting solar cells as a function of the thickness of the layer

In further developments, tuning of the ZnO film and following the insertion of a suitable interface layer, we could manage to thicken the film up to a thickness of 100 nm while preserving a high V_{oc} . As shown in Figure 3. This enables a better optical performance, making such stack promising for high-performance electron-selective contacts (work submitted for publication).

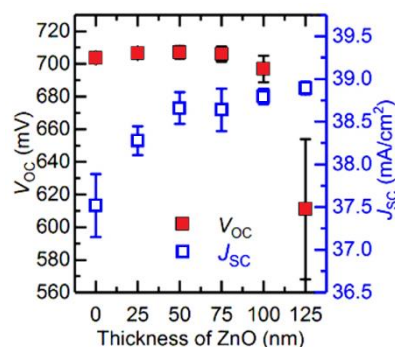


Figure 3 V_{oc} and J_{sc} of 2-side contacted solar cells using a ZnO contact with improved properties as a function of the thickness of the ZnO film.

3.2 Tin oxide (SnO_x)

Another interesting option for electron contacts / transport layers is tin oxide, SnO_x. As a contact material in silicon thin film materials, it has proven its process compatibility and long term stability in such devices.

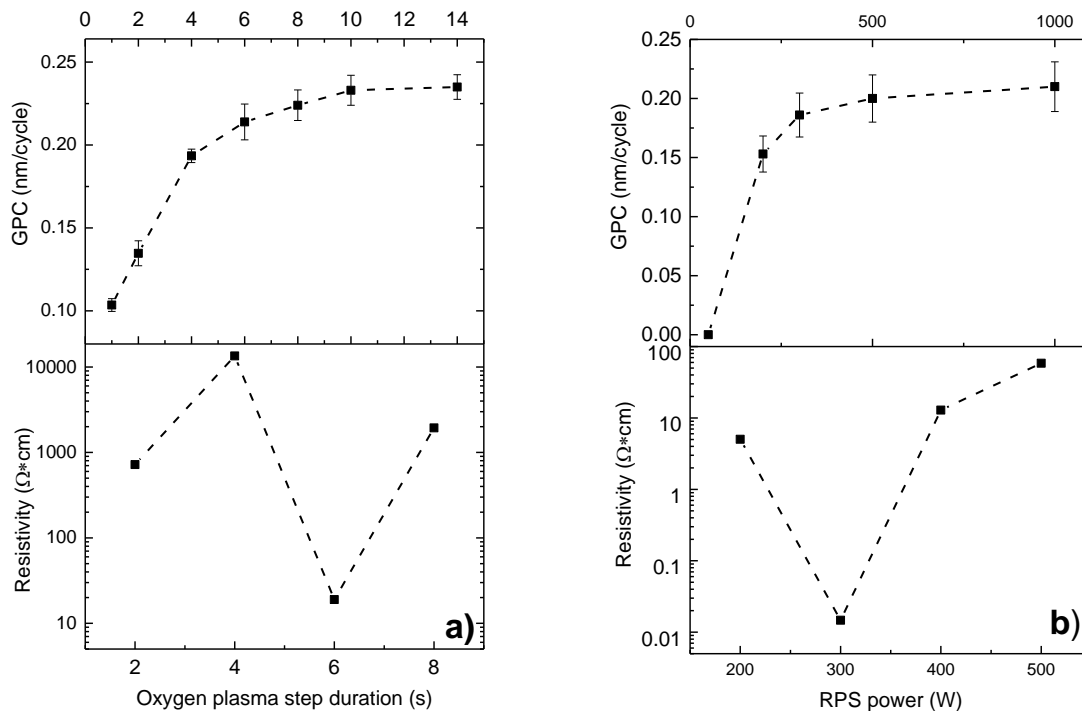


Figure 4 GPC and resistivity of SnO₂ layer as a function of a) oxygen plasma step duration, b) RPS power.

Within NextBase, we have explored the deposition of SnO_x thin films via plasma-enhanced atomic layer deposition (PEALD). Each PEALD sequence consisted of a TDMASn pulse (1.5s)-N₂ purge (5s)-Oxygen plasma (varied duration)-N₂ purge (5s). TDMASn and N₂ pulses were optimized to yield saturation of the film growth per cycle (GPC). However, for the PEALD process the saturation point for the plasma step cannot be adjusted in the same way as for thermal ALD by the step saturation method, mostly due to plasma kinetics. If the reaction kinetic is slow and plasma species are distributed isotropically [4], [5], it is possible to obtain better quality layers before the saturation point. Therefore, the parameters of the oxidation step (pulse time, plasma power) were optimized with regard to conductivity of the SnO₂ layer and not by step saturation. Thus, both saturation point of GPC and resistivity of the layers were investigated simultaneously. Figure 4(a) shows the GPC of SnO₂ layers upon variation of the oxygen plasma step duration. With the short pulses below 4 seconds the growth is reduced, which indicates that such pulse duration is too short for the saturated ALD process. With the increase of the oxygen pulse up to 8-10 seconds, the changes in the GPC are minor, and it can be considered as a saturated process. However, Figure 4(a) shows that the minimal resistivity of the layer can be achieved at 6 seconds of oxygen plasma pulse. Similar optimizations were carried out for the oxygen plasma power, Figure 4(b), for an addition of argon to the precursor gas and for the deposition

temperature (not shown), which allow to further improve the opto-electronic properties of the SnO₂ layers.

Using our EMIL facility at the Berlin synchrotron BESSY II, We have used X-ray and UV photoelectron spectroscopy (XPS, UPS) to investigate the stoichiometry and valence band of our SnO_x films grown on (n)a-Si:H/c-Si substrates, i.e. the relevant structure for silicon heterojunction devices incorporating SnO_x. XPS of the Sn3d core level shows that during the first 10 ALD cycles an intermediate state of tin is present, as evidenced by the appearance of Sn²⁺. During the subsequent formation of the bulk of the film, no Sn²⁺, or metallic Sn⁰ are present in the film, indicating a well-defined SnO₂ film growth.

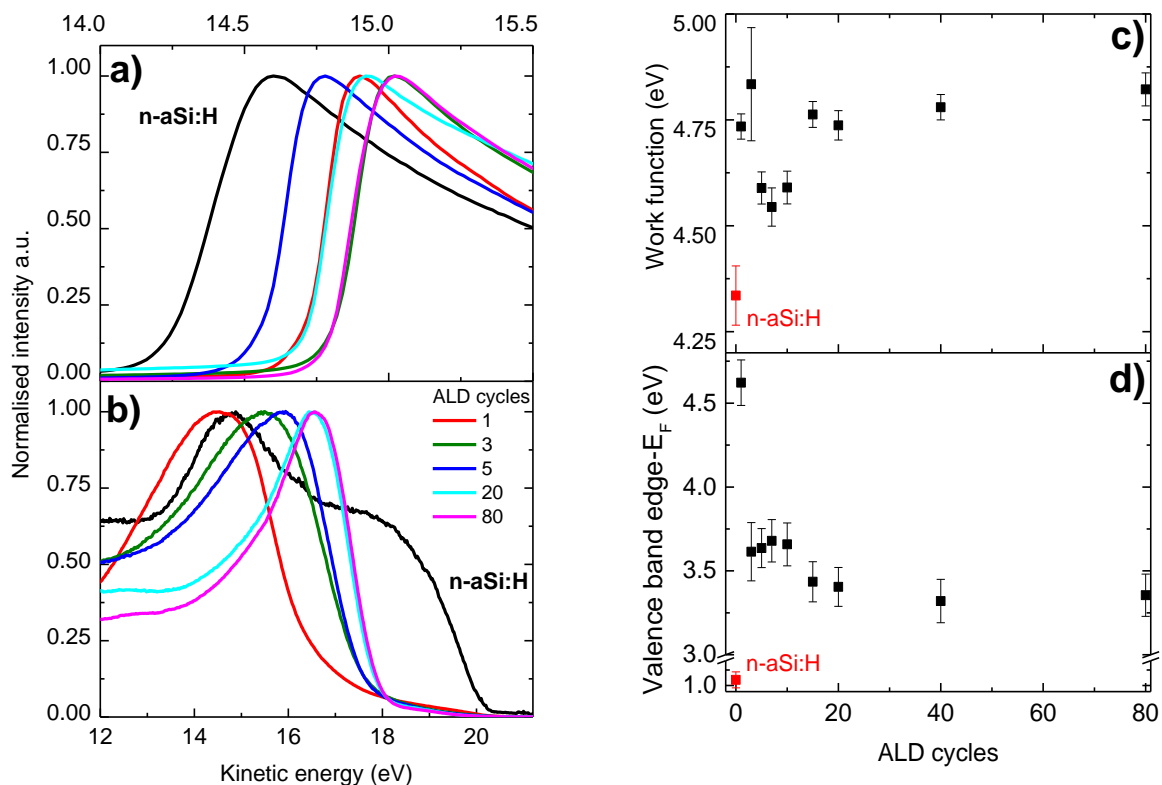


Figure 5 UPS spectra of SnO₂ layers deposited on top of n-doped amorphous silicon and measured after different numbers of ALD cycles. a) secondary cut-off with bias Voltage of 10 V, b) valence band region of the UPS spectra with normalized signal intensity, c) work function of SnO₂ layers on n-aSi:H, d) valence band edge energies relative to E_F as a function of ALD cycles.

Additionally, it was possible to quantify the work function and the valence band edge position of the SnO₂ layers after different growth steps from the UPS measurements. The cut-off region of the UPS spectra and extracted work function values of the layers with increasing number of ALD cycles are shown in Fig. 8, respectively. In both graphs a drastic shift of the work function for the first cycles is apparent, which presumably reflects the oxidation of the silicon surface [6]. During the first 5-10 cycles, the intermediate tin oxide layer is grown, which features a lower work function than the thick SnO₂. However, after 15 cycles the work function stabilizes, which indicates that at this stage the incubation of SnO₂ on the silicon/silicon oxide surface has been completed and the growth has entered a stable

regime. This corresponds to our observations of Sn 3d core level. The work function for the final SnO₂ layer after 80 cycles was measured to be 4.82 eV. That is in the range of literature values, which are between 4.4 and 5.7 eV, depending on the surface state of material [6]. However, this value is higher than reported for other n-type semiconductors, such as ZnO (4.4 eV) [7] or TiO₂ (4.2 eV) [8]. Such high work function can be an issue for using SnO₂ layers as electron contacts in silicon heterojunction solar cells, due to its negative impact on the fill factor, as it was shown in simulations of silicon heterojunction solar cells [9], [10].

Using the method proposed by Kraut *et al.* [11], we were able to estimate the valence band offset at the SnO₂/a-Si:H interface as $\Delta E_v = E_b(\text{SnO}_2) - E_b(\text{Si}) + \Delta E_{CL}$, where $E_b(\text{SnO}_2)$ is the difference between the core level position of Sn⁴⁺ 3d_{3/2} and the valence band edge, $E_b(\text{Si})$ is the difference in core level positions of Si 2p_{1/2} and the valence band edge for bare n-aSi:H substrate and ΔE_{CL} is the difference in core level positions between Sn⁴⁺ 3d_{3/2} and Si 2p_{1/2} in the intermediate state. We find a valence band offset of ~1.8 eV. With the band gaps of a-Si:H and our SnO₂ as determined from spectral ellipsometry, we calculate a substantial conduction band offset of ~0.8-1.0eV, i.e. a substantial barrier which would indeed hinder charge carrier transport of electrons across the SnO₂/a-Si:H interface.

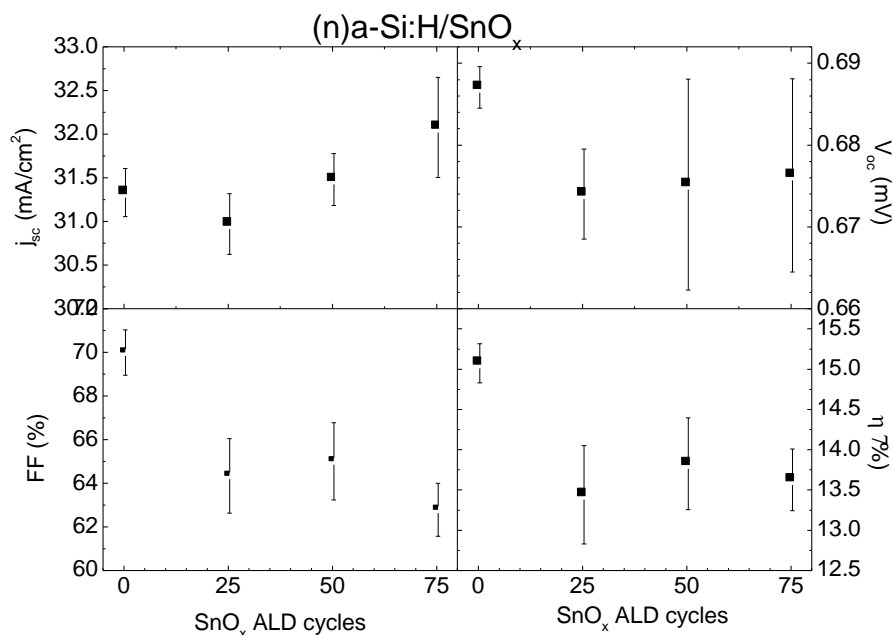


Figure 6 Output of solar cells with c-Si/i-aSi:H/n-aSi:H/SnO₂/ITO rear contact stack, with varied SnO₂ layer thickness at the rear side.

Finally, the optimized layers were applied in silicon solar cells, as part of the electron transport contact, i.e. the layer stack SnO₂/(n,i)a-Si:H implemented as the rear contact of both side contacted cells. As shown in Figure 6, with increased thickness of the SnO₂ layer, both V_{oc} and FF decrease, which confirms the presence of a potential barrier in this stack. Note, that also the reference cells (“0 ALD cycles”) are limited in fill factor due to an optimized top contact & metallization; the low j_{sc} is due to the absence of light trapping since polished wafers were used. Nevertheless, it is clear from both the experimentally determined high conduction band offset and the concomitant poor cell performance, that the

application of SnO₂ in the present configuration is unfortunately not suitable as a non-silicon CSC on crystalline silicon.

3.3 Magnesium oxide (MgO_x)

Another candidate material for electron CSCs in silicon solar cells is magnesium oxide, MgO_x. A water based ALD process using Bis(ethylcyclopentadienyl)magnesium (Mg(CpEt)₂) was investigated to fabricate MgO_x films. This precursor was shown to be a suitable precursor for the growth of high quality MgO layers in the deposition range of 125-200°C, and it can be used in ALD using water as oxidizing agent [12]. In order to see if MgO layers are suitable for the implementation in SHJ solar cells, passivation properties and contact resistance of MgO layers were investigated.

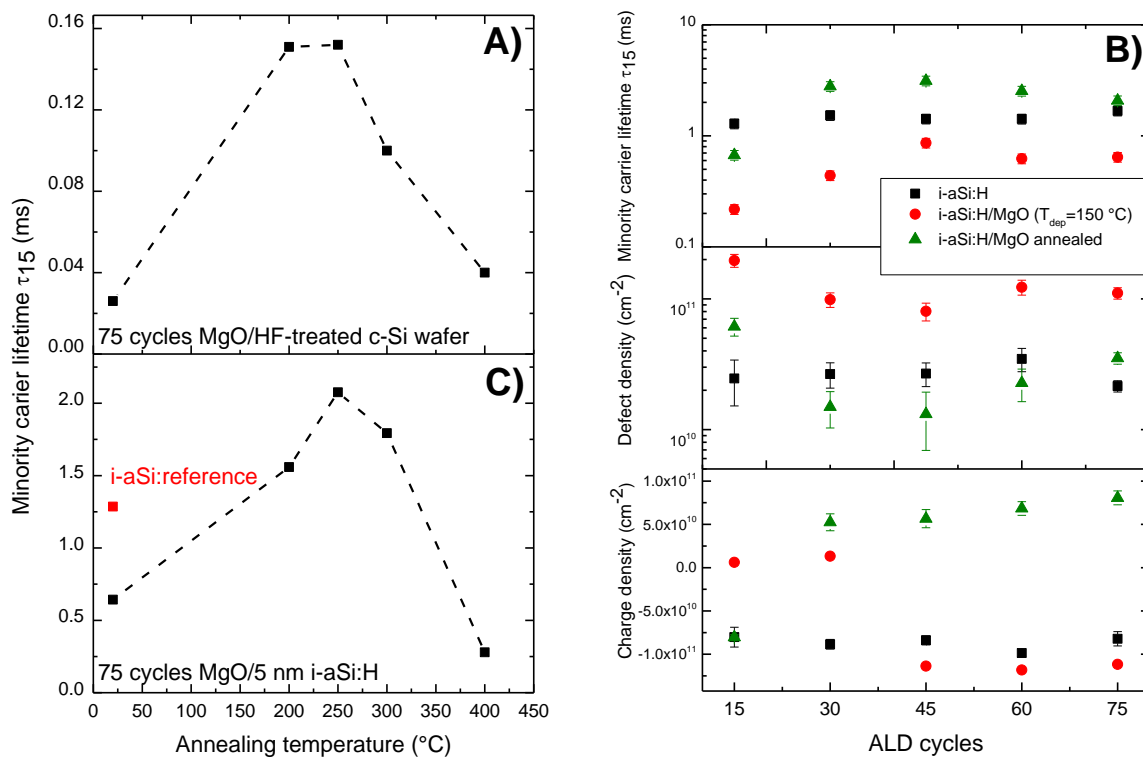


Figure 7 Effective excess minority carrier lifetime at 10^{15} cm^{-3} injection level after MgO layer deposition at 150 °C (a) for the HF-treated c-Si wafer, (c) for i-aSi:H/MgO layer stacks on c-Si as a function of the annealing temperature. (b) Carrier lifetime at 10^{15} cm^{-3} injection level, modelled defect densities and effective charge for i-aSi:H/MgO layer stacks on c-Si substrate, as a function of the number of ALD deposition cycles.

Samples with symmetrical layer stacks on both sides of the wafer were produced in order to investigate changes of the passivation quality in terms of minority carrier lifetime upon deposition of MgO layers. With the direct deposition of a thin MgO layer on c-Si substrates, no passivation was achieved, neither in the as-deposited state, nor after annealing. However, for a thicker MgO layer, i.e. after 75 ALD cycles ($d_{\text{MgO}} \approx 9.8 \text{ nm}$), changes in the passivation quality were observed. Figure 7(a) shows the minority carrier lifetime for such an MgO layer deposited on a c-Si wafer. For the as-deposited stack no passivation is observed. However, after an annealing step of 5 minutes at 200-250 °C, a slight

passivation effect, yielding a lifetime of around 150 μs , is observed. A similar experiment was done with MgO deposited on i-aSi:H coated c-Si substrates. In this case, it was possible to observe significant changes in the effective lifetime with varying MgO thickness. In Figure 7b, the effective minority charge carrier lifetime in c-Si wafers coated with such layer stacks is shown as a function of the number of ALD cycles. After the direct deposition of MgO layer on top of i-aSi:H, there is a noticeable degradation of the lifetime for all MgO layer thicknesses. Using fits of semi-analytical simulation model for minority carrier lifetime [13], [14], we find that this corresponds to the drastic increase in defect density (middle panel in Figure 7b). However, similar to the MgO/c-Si layer stack, the passivation recovery and improvement is observed after an annealing step at 200 °C, with the maximum increase for the sample after 45 MgO ALD cycles, which corresponds to the point with the lowest defect density. At the same time, the total effective charge is slightly increasing with the number of deposition cycles. Therefore, it is possible to conclude that the main c-Si interface passivation mechanism is chemical passivation by the i-a-Si:H film, which degrades upon MgO deposition, then recovers during the annealing step. Additionally, the fixed charge reverses its sign: While it is rather small and negative, $\sim -1 \times 10^{11}/\text{cm}^2$ after i-a-Si:H deposition, it increases to $> +5 \times 10^{11}/\text{cm}^2$ after MgO deposition and anneal, for all MgO thicknesses except the thinnest (15 cycles). This indicates, that MgO/i-aSi:H stacks are indeed suitable as electron contact layers, since the positive fixed charge will lead to a downwards band bending and attract electrons at this contact.

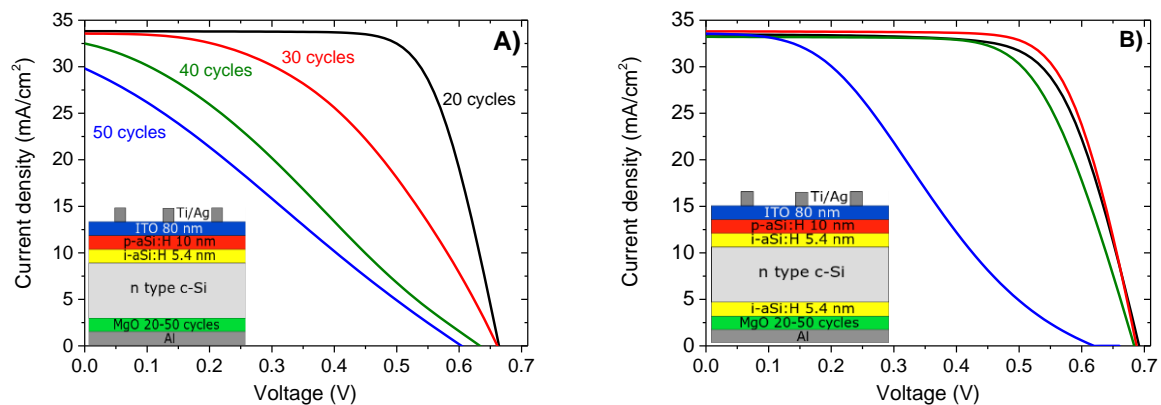


Figure 8 Illuminated one-sun $J(V)$ characteristics for solar cell devices with A) MgO/c-Si layer stack as electron contact on the rear side, B) MgO/i-aSi:H/c-Si stack. The MgO layer thickness was varied. Colors of the curves for both graphs represent the same number of deposition cycles. Schematic representations of the devices are shown as insets.

Sample type	MgO cycles	J_{sc} (mA/cm ²)	V_{oc} (V)	FF (%)	Efficiency (%)
MgO/c-Si	20	33.4	0.664	73.8	16.4
MgO/i-aSi:H	30	33.8	0.687	72.4	16.8
MgO/i-aSi:H*	30	33.7	0.684	75.3	17.3
Reference	0	33.3	0.698	73.4	17.0

Table 2 Solar cell parameters for the best devices fabricated on planar Si wafer incorporating the ALD-grown MgO layers and Al rear contact. *: Ti/Ag instead of Al rear contact.

As a next step, solar cells with MgO/c-Si and MgO/i-aSi:H/c-Si layer stacks as rear contacts on flat (n)-Si wafers were fabricated in order to check the possibility of implementing our ALD layers in the

devices. The MgO layer thickness was varied in the range of 20-50 ALD cycles to see the influence of the layer thickness on the final solar cell performance. In Figure 8 the J(V) characteristics for such devices are shown. Additionally, Table 2 shows the results for the best cell for each type of stack. Due to the flat surfaces of the c-Si wafers used for these cells, the short circuit current is strongly limited. For cells with the MgO/c-Si stack, an efficiency of 16.4 % is achievable with a thin MgO (20 ALD cycles, $d_{\text{MgO}} \approx 2.5$ nm). For comparison, a reference cell with (n,i)a-Si:H contact shows an efficiency of 17%. With a further increase in layer thickness, we observe that a transport barrier is formed, which is reflected in the S-shape of J(V) curves and a decrease of V_{oc} and FF. This degradation is in line with the an increasing contact resistance that was determined on test samples with circular contact pads using the Cox & Strack method. For the MgO/i-aSi:H/c-Si stack, it is obvious that the additional thin i-aSi:H layer helped to keep the passivation on a level that allows V_{oc} s above 680 mV for devices. This shows that the i-aSi:H layer makes it possible to sustain the passivation, and that a thin layer of MgO is sufficient to function as a proper electron transport layer. The slight degradation of the V_{oc} and FF for such stacks as compared to the reference can be attributed to the possible diffusion of aluminum through the MgO stack during the evaporation of the aluminum contact. Indeed, with an alternative metallization consisting of a Ti/Ag stack, an improved efficiency of 17.3% could be demonstrated, outperforming (albeit on this moderate overall level) the reference cell with (n)a-Si as electron contact. Therefore, we conclude that MgOx is a potentially interesting electron-selective contact material for silicon solar cells. However, further device optimizations will be necessary to evaluate its ultimate potential.

4 Hole contact layers

4.1 Tungsten Oxide (WO_x)

HZB's work within NextBase on WO_x as a potential hole-selective contact material started from the encouraging results obtained in a previous EU-funded project, HERCULES (EU FP7). Briefly, the results in that project were obtained on WO_x films that were thermally evaporated in UHV MBE system, where direct photoelectron analysis (XPS, UPS) could be carried out. We could demonstrate, that WO_x with stoichiometries close to WO_3 , yielded work functions close to 6 eV. These were high enough for a hole contact layer, for which we had established a minimal required work function of ~ 5.5 eV. Furthermore, we could show band bendings of up to 600 meV and solar cell fill factors of up to 60% with $WO_x/(i)aSi/cSi$ contact stacks, which could be improved to ~ 700 eV and 70% with an additional (p)a-Si:H interlayer (Figure 9 and [10]). However, it had also become clear that the density of oxygen vacancies was a critical parameter: High O vacancy densities reduce work function, band bending and, finally, solar cell fill factor. Thus, that thermal evaporation was not well suited to this task. Therefore, cell efficiencies remained below those of the (p,i)aSi/(n)cSi reference cells.

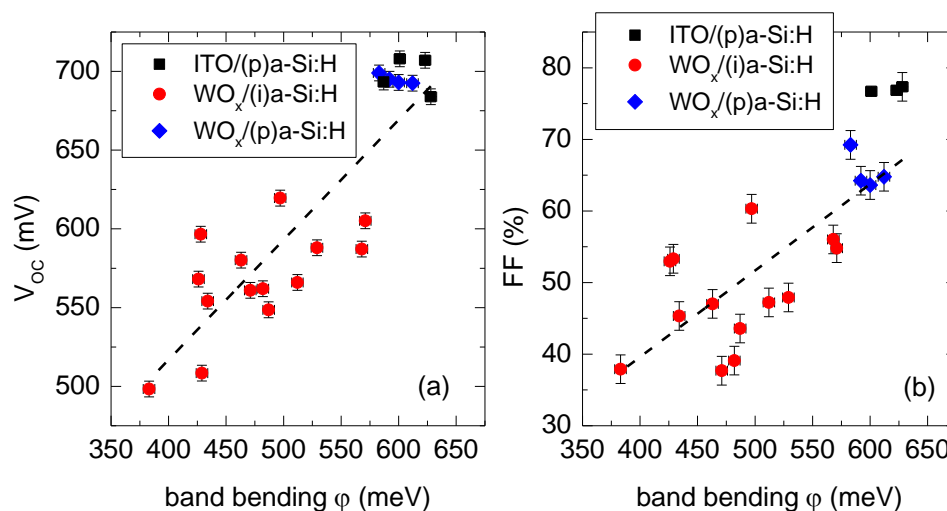


Figure 9. Background – final result of HERCULES (FP7): WO_x/SiH_4 cells with reactively sputtered WO_x films [10].

Sputtered tungsten oxide (WO_x)

Therefore, in NextBase, sputtering of WO_x films was explored as an alternative deposition technique. Here, the stoichiometry can be easily tuned by adding oxygen to the sputter gas; furthermore, sputtering would be a more viable industrial technique.

We find that varying the oxygen gas flow during sputtering enables variation of the WO_x conductivity from $0.01 (\Omega\text{cm})^{-1}$ to $1000 (\Omega\text{cm})^{-1}$ (see Figure 10, left), while the band bending in the interface is changed by 70 meV and iFF of solar cells by 1.5 %. WO_x shows higher resistivity, by about a factor of 10, and higher absorption in the visible range than ITO (Figure 11). Therefore stacks of a thin WO_x film acting as high work function electron-CSC and ITO providing lateral carrier transport antireflection

properties are used in solar cells. It was found that at least 20nm of WOx are required to stabilize the WOx/silicon interface induced band bending, solar cell implied and real FF against the influence of the lower ITO work function.

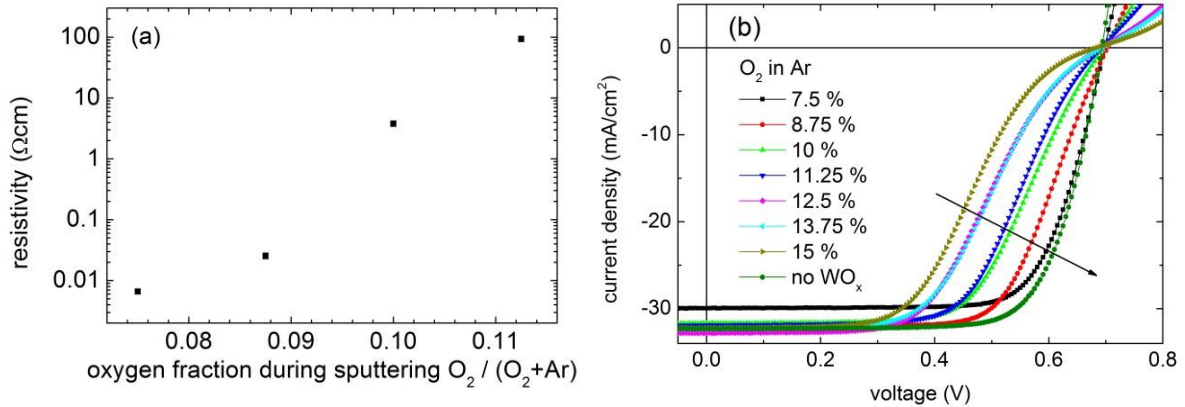


Figure 10: (a) Resistivity of sputtered WO_3 layers plotted versus the oxygen fraction in the sputtering gas. It is possible to vary the conductivity by 3 orders of magnitude depending on the sputtering conditions. (b) $j(V)$ curves of silicon heterojunction solar cells with tungsten oxide hole contacts sputtered using different partial oxygen flows. The high resistivity of layers sputtered at high partial oxygen flows limits the solar cells transport properties.

WOx hole contacts of different thicknesses and conductivity were applied in solar cells (see Figure 10, right) and it was found that the highest FF is achieved with about 20nm thick interlayers of WOx with the highest possible conductivity, meaning the lowest partial oxygen flow during sputtering. It was found that sputtering enables a drastic improvement of WOx/silicon solar cells compared to thermal evaporation, due to the precise control of the WOx conductivity. Unfortunately the resistivity of sputtered WOx is still limiting the FF of these devices.

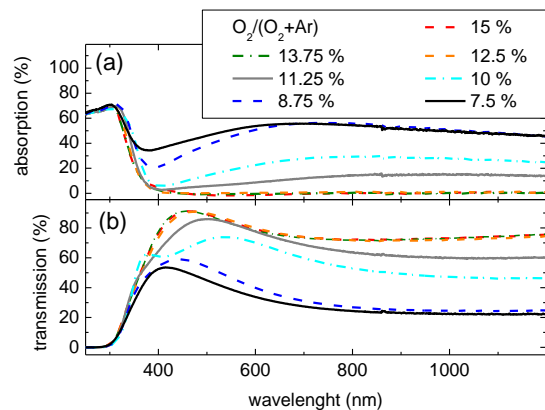


Figure 11. Optical properties of reactively sputtered WO_x films on glass, with varying oxygen concentration during sputtering [15].

Therefore, further experiments were conducted where a precise control of ITO and WOx film thickness was maintained. These experiments were carried out on planar wafers to enable direct control of the deposited thicknesses. The thickness of the overlying ITO was adjusted to maintain a total metal oxide thickness of 80–85 nm. Samples with WOx thicknesses from 0 to 40 nm were prepared using a partial oxygen flow of 8.75%. The results are summarized in Figure 12: In panel (a) it can be seen that 20 nm

of WO_x yields the maximum FF. For higher WO_x thicknesses the FF is decreasing because of the high series resistance of the WO_x layers. For thicknesses below 20 nm, the FF is lower, because the low ITO work function is projected through the WO_x and onto the interface to (p)a-Si:H, as evidenced by c-Si band bending extracted from surface photovoltage measurements on reference samples. Unfortunately, the WO_x solar cells show lower FFs than the reference solar cells without WO_x, which reveals that the high resistivity of WO_x is still limiting these solar cells.

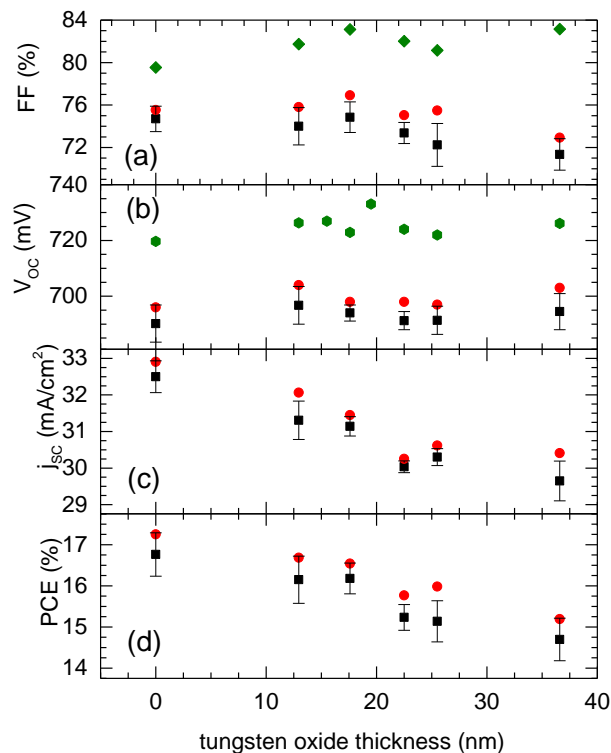


Figure 12. Dependence of solar cell parameters on tungsten oxide thickness for SHJ cells with WO_x/(i)a-Si:H front contact. The cells were fabricated on planar (100) wafers and have the structure ITO/WO_x/(p,i)a-Si:H/(n)c-Si/(i,n)a-Si:H/ITO. Black squares with ranges mark average values with the standard deviation of the 12 cells on each respective wafer. Red circles mark the maximum value of each wafer and green circles mark the implied FF and implied V_{oc} from photoconductance decay measurements performed after ITO deposition [15].

The decreasing trend in cell efficiency vs. WO_x thickness, Figure 12 (d), is dominated by the decreasing j_{sc}, (panel (c)). This is mostly because WO_x sputtered at 8.75% partial oxygen flow has a higher parasitic absorption than ITO. Indeed, the highest efficiency of 16.7% is obtained for the thinnest (11 nm) WO_x.

To sum up our findings, the conductivity of these sputtered and not intentionally doped WO_x films is about one order of magnitude below that of typical transparent conductive oxides, while the parasitic absorption is higher than in, e.g., ITO. Therefore, WO_x was applied in stacks with ITO in this study. It was found that about 16–18 nm of WO_x is necessary to benefit from the high WO_x work function and prevent a detrimental influence of the lower ITO work function on the interface between WO_x and silicon. The best solar cell using WO_x as the hole contact and thus not having any p-doped layer showed 16.6% efficiency. The WO_x in this solar cell was prepared using 7.5% oxygen in the sputter gas and had

a resistivity of about 0.01 Ω/cm . Additionally, using WO_x as an interlayer between p-type amorphous silicon and ITO lead only to efficiencies comparable to but below the reference solar cells. All solar cells showed higher implied FFs than the corresponding cells without WO_x . However, it was not possible to transfer this high implied FF into a device. The main reason for this is the high series resistance of WO_x and an overall lower band bending for WO_x layers with higher conductivity. Thus, it was shown that sputtering of WO_x enables decent control of its conductivity and stoichiometry, but the overall conductivity of these layers is still too low to enable highly efficient hole contacts on silicon. These results were published in IEEE J. Photovoltaics [15].

PEALD-deposited Tungsten Oxide

Similar to the PEALD deposition of SnO_x reported above, we also investigated an alternative tungsten oxide deposition process using plasma-assisted processes. WO_x was grown from a $\text{W}(\text{CO})_6$ precursor. The deposited layers showed no traces of carbon contamination, and exhibit work functions of ≈ 5.5 - 5.75 eV. However, due to the non-uniform distribution of oxygen plasma in the chamber, the thickness distribution is highly inhomogeneous on the different positions of the substrate.

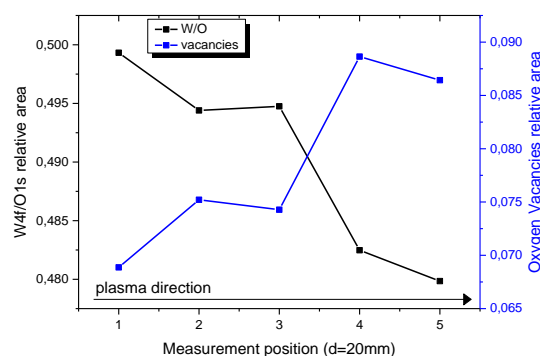


Figure 13 Relative area ratio W 4f/O 1s core level (black), Relative area of oxygen vacancies in W 4f core level (blue) as function of a distance from the plasma source

Additionally, with XPS measurements it was possible to monitor that not only the thickness, but also the stoichiometry of the layer varies slightly. The change of the stoichiometry with changing distance from the plasma source is presented in Figure 13. We find, that only W^{6+} species are present in the W 4f core level; the change of stoichiometry is caused by the increase of oxygen vacancies with an increase of the distance from the plasma source. Thus, further process optimization is required in order to obtain fully stoichiometric films irrespective of sample position in a proper ALD process.

PEALD deposited WO_x layers are implemented as a front emitter for the SHJ solar cells, with a front stacking sequence of ITO/ WO_x /(i)aSi/(n)cSi and varying WO_x thickness. As seen from Figure 14, S-shapes are observed in illuminated I-V curves. Accordingly, as listed in Table 3, low V_{oc} s with low fill factors (FF) for all WO_x layer thicknesses (varying number of ALD cycles) are observed. On the other hand, the passivation of the structure remained on a high level, and is comparable with the reference structures, as observed from TRPCD and PL measurements. However, the final V_{oc} of the device shows a drastic drop from expected measured i- V_{oc} (>710 mV). Therefore, further investigation is needed in

order to estimate possible effects of barriers at the interfaces and/or low film conductivities and loss of charge carrier selectivity.

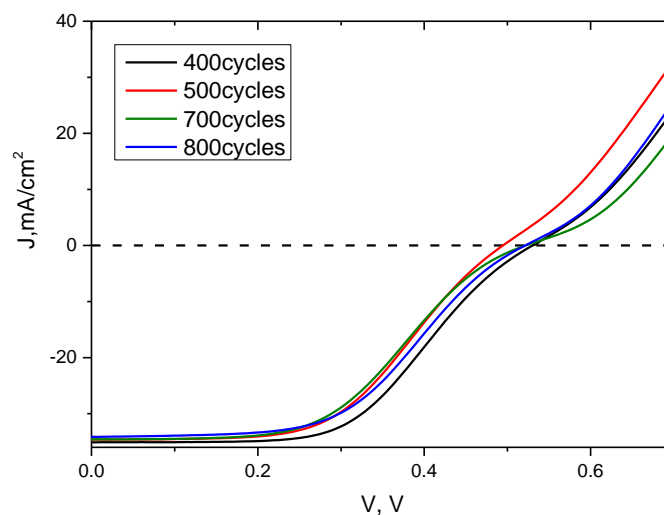


Figure 14 IV Solar cell performance with WOx layer, as a hole-selective layer for different ALD cycles

Table 3 Solar cell performance with WOx as a hole-selective layer for increasing no. of ALD cycles

WOx ALD cycles	Average Jsc, mA	Average Voc, mV	Average FF, %	Average Eff, %
400	-34,8	514	51,0	9,1
500	-34,6	492	48,9	8,3
600	-34,5	503	46,0	8,0
800	-33,7	510	46,8	8,1

4.2 Indium Tungsten Oxide (IWOx)

In a next step, we investigated novel mixtures of tungsten oxide (high WF, low conductivity) and indium oxide (low WF, high conductivity) in order to find a trade-off between high work function and high conductivity. If the conductivity of the layers is good enough, even a carrier selective TCO might be possible. We investigated the full range from pure tungsten oxide to pure indium oxide. We used thermal evaporation as deposition method with various temperatures for the tungsten oxide and indium oxide sources. The relative amount of indium and tungsten oxide was measured using X-ray photoelectron spectroscopy (cf. Figure 15).

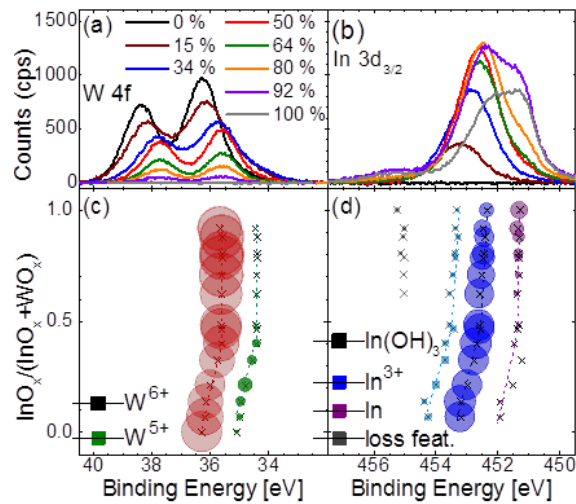


Figure 15. Electron core levels of tungsten (W 4f) and Indium (In 3d) for samples with various amounts of indium oxide and tungsten oxide in the mixture. The respective binding energy and intensity of the core level components are shown in panels c and d. [16]

Additionally the work function of all these mixtures were investigated using He-UPS. The measured work functions ranged from 6.25 eV (tungsten oxide) to about 4.25 eV (indium oxide). We found that tungsten oxide features the highest work functions and induces the strongest band bending into crystalline silicon. Both values decrease continuously with increasing indium content. However, the measured band bending is much lower than the Anderson Model [17] predicts for such a large difference in work function. The pinning factor of non-passivated Silicon is known to be close to $S=0.1$ [18], which we observe here as well. Additionally we investigated the band gaps of these layers by means of optical spectroscopy and found a slight decrease of the band gap with increasing indium oxide content, which is concomitant with a shift of the valence band towards the Fermi level, E_F , which again was measured by means of He-UPS.

Figure 16 shows the mentioned data in combination as the band alignment vs. varying InO_x content, plotted relative to the Fermi level (E_F). The work function is the most prominent change in the band alignment. The band gap and the valence band edge decrease only slightly about 0.4 eV by following the same trend. Hence, the energetic position of the conduction band stays constant about +0.3 eV above the Fermi level, whereas the valence band approaches the Fermi level from -3.5 eV for pure WO_x to -3.18 eV for pure InO_x .

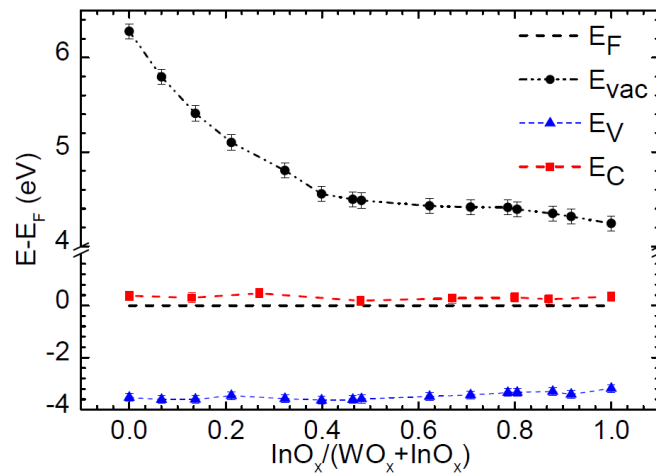


Figure 16. Band alignment of IWOx thin films on silicon plotted versus the InOx content in the mixture of indium oxide and tungsten oxide. The vacuum energy (E_{vac}), the valence (E_V) and conduction band edge (E_C) position are reported relative to the Fermi-level (E_F) and plotted versus the fraction of InOx in the IWOx alloy. [16]

For further evaluation we discuss the heterojunction of the metal oxide mixtures with crystalline silicon ($E_G=1.12$ eV, electron affinity = 4 eV, work function $WF = 4.3$ eV, for present dopant concentration) shown in Figure 17. The conduction of carriers in these high-work-function metal oxides is facilitated by defect states close to E_F and the offset between the Fermi-level in WO_x and the valence band of c-Si is only 210 meV, which can be overcome by thermionic emission. Therefore, although strong Fermi level pinning is observed, the tungsten-oxide-rich mixtures should be suitable as hole-selective contact for crystalline silicon.

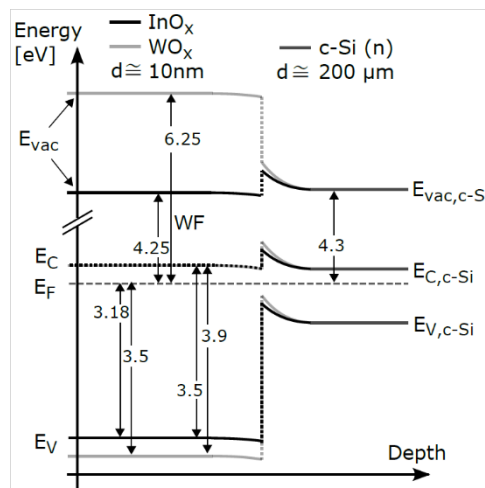


Figure 17. Sketch of the heterojunction between WO_x (grey line)/ InO_x (black line) and n-type c-Si (dark grey line) with work function (WF), valence band edge (VB) and band gap (EG). Values for WO_x and InO_x values obtained using He-UPS, optical spectroscopy and surface photovoltage and values for c-Si were taken from literature with a donor density of 10^{15}cm^{-3} . [16]

The indium-oxide-rich mixtures show a significantly lower band bending, which leads to a larger offset to the Fermi level in the metal oxide and additionally to a less pronounced carrier selectivity, since the rejecting barrier for the electrons in the conduction band of the c-Si is smaller. Comparing the offset

in the vacuum energy levels at the $\text{InO}_x/\text{c-Si}$ and $\text{WO}_x/\text{c-Si}$ interface, an inversion of the surface dipole charge is observed.

First experiments of thermally evaporated (I) WO_x applied as hole selective contact in silicon heterojunction (SHJ) solar cells showed moderate results with mainly difficulties in charge carrier extraction, leading to strong S-shapes in the IV-curves as seen in Figure 18 for a thickness variation of pure tungsten oxide as hole selective contact.

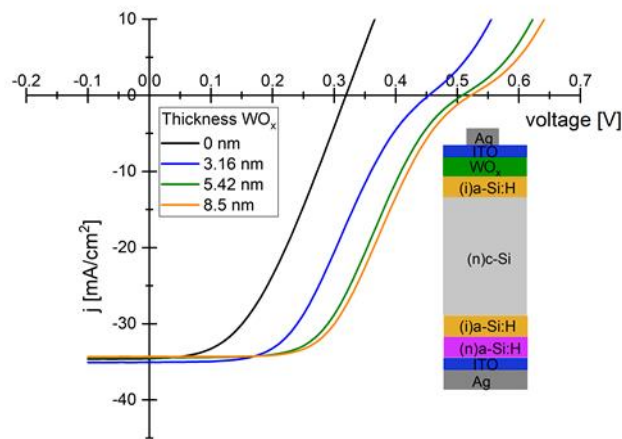


Figure 18. IV-Measurement of Heterojunction solar cells with different thicknesses of thermal evaporated tungsten oxide as p-contact

A second series aimed for a well suited trade-off between the high-work function WO_x and the highly conductive InO_x , where a layer with $C_{\text{In}}=16\%$ InO_x -content in the mixture showed the most promising results. Hence, a thickness variation with $C_{\text{In}}=15\%$ InO_x -content in the mixture was conducted, but showed the same problems with extraction barriers. The layer stack is the same as shown in Figure 18 with IWO_x instead of pure WO_x . The obtained AM1-5-illuminated I-V parameters of both thickness variations are shown in Figure 19 for different thicknesses of the applied metal oxide contact. The cells with pure tungsten oxide showed a slightly higher fill factor, which might be due to better selectivity,

because of the higher band bending as seen above. Still, best FF values are of the order of 50% only. Furthermore, the passivation quality is not good enough to reach reasonable open circuit voltages.

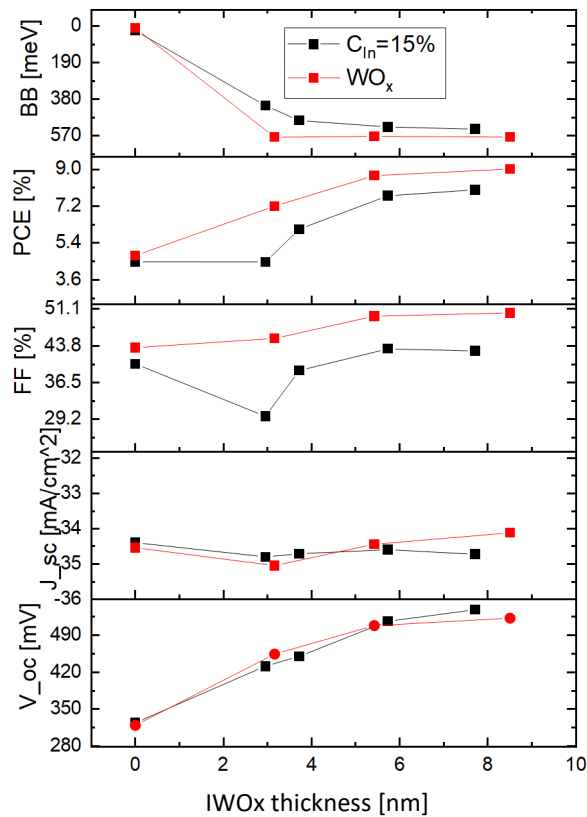


Figure 19. IV-Parameters of two cell-series: One with pure tungsten oxide as hole selective contact and the other one with 15% indium oxide in the mixture. The thickness of the (I)WO_x was varied for each series.

To conclude this section, we find that despite an encouraging tunability of the IWO_x work function by changing the indium content in the film, it was not possible to obtain decent solar cell results using IWO_x/(i)a-Si:H/c-Si hole contacts. The reasons are probably twofold: a) Fermi level pinning at the IWO_x/Si interface causing low band bending and a barrier to hole transport at the heterointerface, and b) degradation of the aSi/cSi interface upon IWO_x deposition, as evidenced by the low V_{oc}s.

5 Summary of experimental results

The results presented in the preceding chapters on the development of different electron- and hole-selective contacts are summarized in Table 4 together with some relevant material parameters, and with solar cell efficiencies where applicable.

Table 4. Summary of the most important electronic properties of the metal oxides investigated by NextBase consortium partners, and efficiencies of solar cells processed with these layers.

Material	Use as	Work function [eV]	Band bending* [meV]	Conductivity [S/cm]	Best cell efficiency [%]	Comments
SnO _x	n-CSC, TCO	4.82 (150 °C PEALD) 4.3 (120 °C water)	72	5.6*10 ⁻³ PEALD 10 ⁻³ (80°C water)	14.2	ALD [23]
MgO _x	n-CSC				17.3 with (i)a-Si:H - Ti/Ag metallization; 16.4 without (i)a-Si:H	ALD
WO _x	p-CSC	6.4	625	< 10 ⁻⁶	16.6	sputtered [15]
WO _x	p-CSC	5.5-5.75	500	1.5*10 ⁻⁵	9.1	PEALD
IWO _x	p-CSC	6.4-4.3	600-400	InOx: 1; WOx: 10 ⁻⁴ ; IWOx: ~10 ⁻⁵	14.2 (@ 16%InOx)	Thermal co-evap. of InOx and WOx [16]
NiO _x	p-CSC			<~10 ³		Ni e-beam in O ₂
AZO	n- CSC	3.9		28 – 65	19.5	Magnetron sputtered ~2-nm-thick, in combination with passivating (i)a-Si:H and Al [24]
MgF ₂	n- CSC	3.5		< 10 ⁻⁶	20.5	Evaporated ~1.6-nm-thick, in combination with passivating (i)a-Si:H and Al

As can be seen from the table, although the work functions of the investigated materials are suitably high (for hole contact materials) or low (for electron contact materials), they mostly do not translate into high band bendings on (n)c-Si wafers. Furthermore, the conductivities are rather moderate, therefore the films would not be suitable as a front side TCO in both-side contacted cells. However, the conductivity is sufficient for application in IBC cells, where good lateral conductivity is provided by the metallization. Furthermore, it was found that the TMOs do not passivate c-Si wafers sufficiently to

allow for high V_{oc} s, with the possible exception of MgOx (minority carrier lifetime $\sim 150 \mu\text{s}$ demonstrated for MgOx/(n)c-Si samples after anneal in a not fully optimized process). Thus, a PECVD-deposited intrinsic amorphous silicon layer, (i)aSi:H, is necessary in all cases, which further increases contact resistance. Therefore, the cell results are limited to fill factors well below 80% and V_{oc} s $< 720 \text{ mV}$. The currently best IBC-SHJ cell with non-silicon CSCs processed within NextBase uses a full area (i)a-Si:H passivation processed at $200 \text{ }^\circ\text{C}$, followed by a sequence of two shadow-masked evaporation steps at room-temperature: MoO_x/Ag for the hole- and $\text{MgF}_x/\text{Mg}/\text{Al}/\text{Ag}$ for the electron-selective contact as presented in chapter 2. It exhibits the following device parameters, measured at STC: V_{oc} 709 mV, j_{sc} $41.5 \text{ mA}/\text{cm}^2$, FF 75.6%, and a power conversion efficiency of 22.2% [2]. This world-record efficiency for non-silicon-contacted device is remarkable—yet way underperforming compared to silicon-based contacting approaches.

6 Risks and interconnections

6.1 Risks/problems encountered

When setting up the NextBase project, the work in WP4 – particularly the exploratory work of TMOs in T4.2 – were planned as a potentially high benefit study to improve cell performance. T4.2 was seen as a risk mitigation strategy regarding contact resistance issues in IBCs that were expected to become more severe when the contacts for both charge polarities have to share the rear side of the wafer. However, the work on PECVD-a-Si:H and nc-Si:H-based contacts for IBC-SHJ has made very good progress (cf. progress and deliverable reports for WPs 5 & 6). Indeed, these materials have proven to be suitable for Vocs well above 700mV and a FF potential beyond 80% (D4.1, M24), and have therefore been selected as contact materials for WP 5 & 6 (MS 2, at M24). Thus, progress in the “conventional” silicon-based contact strategies make the use of alternative contact layers a lower priority. Deliverables D4.1 and D4.2 could thus have been linked at the proposal stage as being two options for the same objective, as fulfilling one is enough for project success. Also, it turned out that although the objectives of this deliverable (V_{oc} and FF) make sense for the final device objective, since this deliverable reflects work on layer properties, a metric based on layer properties (typically targeting the passivation and contact resistivity required to enable the V_{oc} and FF metrics that were chosen here) would have been preferable. Such insights are very valuable for future project writing. Overall, these difficulties and the failure in demonstrating excellent solar cell properties with TMO-based contacts are not precluding the main goals of the NextBase project to be reached, in particular the 26%-efficiency at the cell level and 22%-efficiency at the module level.

6.2 Interconnections with other deliverables

This deliverable is related to the following deliverables/milestones/tasks:

- Deliverable D4.1: “IBC devices employing a-Si:H and c-Si:H based contact stacks with $V_{oc}>740$ mV and $FF>82\%$ ” [M24].
- Milestone 2: “Selection of most suitable front stack and back contact system” [M24].
- Task 4.2: “Development and optimization of novel TMOs for selective contacts”.

7 Conclusions

The goal of this deliverable was to demonstrate the implementation of alternative charge selective junctions using transition metal oxides (TMOs) in highly efficient IBC silicon heterojunction solar cells, in order to improve cell performance by reducing transport losses. Furthermore, we were aiming at exploring different deposition techniques such as sputtering, thermal evaporation or ALD, which might provide cost advantages over conventional PECVD-deposited a-Si:H contacts.

During the project, considerable effort was devoted to both understanding the basic materials properties and implementing optimized films into solar cells, and new insights into the physics of these materials were generated. However, the best cell results for all-TMO IBC SHJ cells fall short by 31 mV and 6.4%, respectively, of the V_{oc} of 740 mV and FF of 82% envisaged for the deliverable. This is mainly due to the limitations of TMO materials properties, while the developed processes – e.g. the shadow mask process mentioned above for the current best cell, or photolithography for e.g. ALD-based films – are in principle well suited to process highly efficient cells. Note that these findings are in line with results reported by other groups in literature; notably, to our knowledge, fill factors above 80% have not been demonstrated with all-TMO-based SHJ cells. The studies summarized above have still yielded a wealth of useful information on the properties of these materials and their interfaces to Si and the metal contacts, as also demonstrated by the peer-reviewed publications referenced in Table 4. Furthermore, it has become very clear that such TMO films are not only interesting for SHJ cells, but also as contact materials for perovskite solar cells and as cell interconnect in the emerging perovskite/silicon tandem cells and other potential next-generation photovoltaic devices. Thus, these studies are expected to have an impact beyond the NextBase project and to pave the way for future developments.

8 References

- [1] J. Bullock *et al.*, “Efficient silicon solar cells with dopant-free asymmetric heterocontacts,” *Nat. Energy*, vol. 1, p. 15031, 2016.
- [2] W. Wu *et al.*, “22% efficient dopant-free interdigitated back contact silicon solar cells,” in *AIP Conference Proceedings*, 2018, vol. 1999, no. 1, p. 40025.
- [3] J. Bullock *et al.*, “Stable Dopant-Free Asymmetric Heterocontact Silicon Solar Cells with Efficiencies above 20%,” *{ACS} Energy Lett.*, vol. 3, no. 3, pp. 508–513, Jan. 2018.
- [4] J. L. Van Hemmen *et al.*, “Plasma and Thermal ALD of Al₂O₃ in a Commercial 200 mm ALD Reactor,” *J. Electrochem. Soc.*, vol. 154, no. 7, pp. G165–G169, 2007.
- [5] H. B. Profijt, S. E. Potts, M. C. M. van de Sanden, and W. M. M. Kessels, “Plasma-Assisted Atomic Layer Deposition: Basics, Opportunities, and Challenges,” *J. Vac. Sci. Technol. A Vacuum, Surfaces, Film.*, vol. 29, no. 5, p. 050801, 2011.
- [6] A. Klein *et al.*, “Surface potentials of magnetron sputtered transparent conducting oxides,” *Thin Solid Films*, vol. 518, no. 4, pp. 1197–1203, 2009.
- [7] L. Korte, R. Rößler, and C. Pettenkofer, “Direct determination of the band offset in atomic layer deposited ZnO/hydrogenated amorphous silicon heterojunctions from X-ray photoelectron spectroscopy valence band spectra,” *J. Appl. Phys.*, vol. 115, no. 20, 2014.
- [8] A. Imanishi, E. Tsuji, and Y. Nakato, “Dependence of the work function of TiO₂ (Rutile) on crystal faces, studied by a scanning auger microprobe,” *J. Phys. Chem. C*, vol. 111, no. 5, pp. 2128–2132, 2007.
- [9] K. U. Ritzau *et al.*, “TCO work function related transport losses at the a-Si:H/TCO-contact in SHJ solar cells,” *Sol. Energy Mater. Sol. Cells*, vol. 131, pp. 9–13, 2014.
- [10] M. Mews, L. Korte, and B. Rech, “Oxygen vacancies in tungsten oxide and their influence on tungsten oxide/silicon heterojunction solar cells,” *Sol. Energy Mater. Sol. Cells*, vol. 158, pp. 77–83, 2016.
- [11] E. A. Kraut, R. W. Grant, J. R. Waldrop, and S. P. Kowalczyk, “Precise Determination of the Valence-Band Edge in X-Ray Photoemission Spectra: Application to Measurement of Semiconductor Interface Potentials,” *Phys. Rev. Lett.*, vol. 44, no. 24, pp. 1620–1623, 1980.
- [12] B. B. Burton, D. N. Goldstein, and S. M. George, “Atomic layer deposition of MgO using bis(ethylcyclopentadienyl)magnesium and H₂O,” *J. Phys. Chem. C*, vol. 113, no. 5, pp. 1939–1946, 2009.
- [13] C. Leendertz, N. Mingirulli, T. F. Schulze, J. P. Kleider, B. Rech, and L. Korte, “Discerning passivation mechanisms at a-Si:H/c-Si interfaces by means of photoconductance measurements,” *Appl. Phys. Lett.*, vol. 98, no. 20, 2011.
- [14] C. Leendertz, R. Stangl, T. F. Schulze, M. Schmidt, and L. Korte, “A recombination model for a-Si:H/c-Si heterostructures,” *Phys. Status Solidi Curr. Top. Solid State Phys.*, vol. 7, no. 3–4, pp. 1005–1010, 2010.
- [15] M. Mews, A. Lemaire, and L. Korte, “Sputtered Tungsten Oxide as Hole Contact for Silicon Heterojunction Solar Cells,” *IEEE J. Photovoltaics*, vol. 7, no. 5, pp. 1209–1215, 2017.
- [16] D. Menzel, M. Mews, B. Rech, and L. Korte, “Electronic structure of indium-tungsten-oxide alloys and their energy band alignment at the heterojunction to crystalline

- silicon,” *Appl. Phys. Lett.*, vol. 112, no. 1, pp. 1–5, 2018.
- [17] R. L. Anderson, “Germanium-Gallium Arsenide Heterojunctions [Letter to the Editor],” *IBM J. Res. Dev.*, vol. 4, no. 3, pp. 283–287, 1960.
- [18] W. Mönch, *Electronic Properties of Semiconductor Interfaces*. Springer, Berlin, 2004.
- [19] T. Abzieher *et al.*, “Electron-Beam-Evaporated Nickel Oxide Hole Transport Layers for Perovskite-Based Photovoltaics,” *Adv. Energy Mater.*, vol. 0, no. 0, p. 1802995, 2019.
- [20] F. Lang *et al.*, “Perovskite Solar Cells with Large-Area CVD-Graphene for Tandem Solar Cells,” *J. Phys. Chem. Lett.*, vol. 6, no. 14, pp. 2745–2750, 2015.
- [21] R. Islam, P. Ramesh, J. H. Nam, and K. C. Saraswat, “Nickel oxide carrier selective contacts for silicon solar cells,” in *2015 IEEE 42nd Photovoltaic Specialist Conference (PVSC)*, 2015, pp. 1–4.
- [22] F. Menchini *et al.*, “Application of NiOx thin films as p-type emitter layer in heterojunction solar cells,” *Phys. status solidi*, vol. 13, no. 10–12, pp. 1006–1010, 2016.
- [23] G. Chistiakova, M. Mews, R. G. Wilks, M. Bär, and L. Korte, “In-system photoelectron spectroscopy study of tin oxide layers produced from tetrakis(dimethylamino)tin by plasma enhanced atomic layer deposition,” *J. Vac. Sci. Technol. A Vacuum, Surfaces, Film.*, vol. 36, no. 2, p. 02D401, 2018.
- [24] S. Zhong *et al.*, “Exploring co-sputtering of ZnO:Al and SiO₂ for efficient electron-selective contacts on silicon solar cells,” *Sol. Energy Mater. Sol. Cells*, vol. 194, no. February, pp. 67–73, 2019.